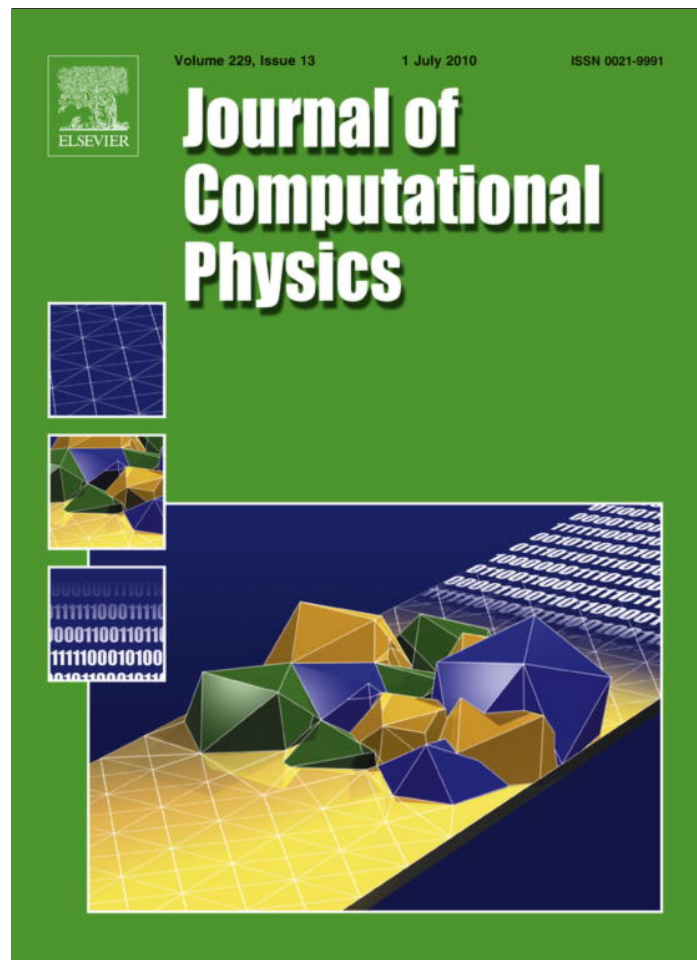


Provided for non-commercial research and education use.
Not for reproduction, distribution or commercial use.



This article appeared in a journal published by Elsevier. The attached copy is furnished to the author for internal non-commercial research and education use, including for instruction at the authors institution and sharing with colleagues.

Other uses, including reproduction and distribution, or selling or licensing copies, or posting to personal, institutional or third party websites are prohibited.

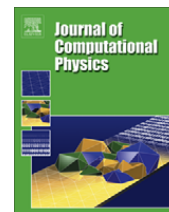
In most cases authors are permitted to post their version of the article (e.g. in Word or Tex form) to their personal website or institutional repository. Authors requiring further information regarding Elsevier's archiving and manuscript policies are encouraged to visit:

<http://www.elsevier.com/copyright>



Contents lists available at ScienceDirect

Journal of Computational Physics

journal homepage: www.elsevier.com/locate/jcp

Regularizing a vortex sheet near a separation point

Silas Alben

School of Mathematics, Georgia Institute of Technology, 686 Cherry Street, Atlanta, GA 30332-0160, United States

ARTICLE INFO

Article history:

Received 30 April 2009

Received in revised form 25 March 2010

Accepted 30 March 2010

Available online 4 April 2010

Keywords:

Fluid

Vorticity

Flow

Kutta

Vortex sheet

Smoothing

Regularization

ABSTRACT

Current methods for computing vortex sheet separation use a regularization parameter which is discontinuous from the body to the vortex sheet. We propose two methods for reducing the errors associated with the discontinuity and improving convergence with respect to the regularization parameter. The “velocity smoothing” method is the simpler of the two, and removes the discontinuity in regularization from one of the two equations where it occurs. The “tapered smoothing” method removes the discontinuity from both equations. In a model problem, both methods are found to converge much more rapidly (with exponents $3/2$ and 2 versus $1/2$ for the standard method) as the regularization parameter tends to zero. Unsteady algorithms are proposed for evolving the free sheet using the two methods, and are tested in a benchmark problem. Accuracy is significantly improved for similar computational expense.

© 2010 Elsevier Inc. All rights reserved.

1. Introduction

In a generic laminar high-Reynolds-number flow near a solid surface, a thin boundary layer of large vorticity forms at the surface. In the limit of infinite Reynolds number (or zero dimensionless viscosity), the boundary layer width shrinks to zero. It is then called a “vortex sheet” [1], and is a line distribution of vorticity in a two-dimensional flow. On a solid surface, the vortex sheet strength distribution is determined by the condition that fluid does not penetrate the body together with a condition on the total vorticity (or circulation) present on the body. For a sharp-edged body such as a Joukowski airfoil, the classical Kutta condition determines how the flow speed at the sharp edge can be made finite by the flux of vorticity from the body into the flow at the sharp edge, which is known as “separation” [2]. Recently, Jones has developed a general computational method for the separation of vortex sheets from a rigid plate with prescribed motion [3]. This work builds on previous work by Krasny on computational methods for the dynamics of isolated vortex sheets [4,5] and vortex sheets shed from a rigid plate [6]. In [7], Nitsche and Krasny simulated the axisymmetric vortex sheet shed from a rigid body (a piston tube). They obtained very good agreement with experiments in terms of the detailed shapes of the vortex sheets as they rolled up into vortex rings, which was an important validation for these models of vortex sheet separation. Regularization of the vortex sheet using a smoothing parameter is a common element of these studies, and was used in earlier work by Chorin and Bernard [8]. Regularization is one of the most robust approaches for preventing numerical instabilities in simulations of vortex sheets; [5] lists some of the alternative approaches which have developed since the early simulation of Rosenhead [9]. The method for rigid bodies was afterwards extended to deforming bodies with motions which are prescribed [10,11] or fully coupled to the fluid [12,13].

A more approximate model lumps the vorticity from the sheet into a small number of discrete point vortices, the strength of which varies in time according to the Kutta condition [14–16]. Separation from a smooth surface (a cylinder) has also been

E-mail address: alben@math.gatech.edu

studied using a vortex sheet model [17]. In this case the location of separation becomes an additional unknown to be solved for at each time step.

The convergence rate as the regularization parameter δ is taken to 0 was studied in some detail by Krasny for isolated vortex sheets [4]. For vortex sheets separating from a solid body, the convergence behavior as $\delta \rightarrow 0$ was addressed by Nitsche and Krasny [7], Nitsche [18], and Shukla and Eldredge [10]. However, these works did not report the convergence rate. The present work provides a detailed study of the convergence rate and methods for its improvement. We first investigate the convergence rate with respect to δ for vortex sheets separating from a plate with sharp edges. We then propose two numerical methods which decrease the error due to δ , relative to existing methods, in the creation and dynamics of vorticity. In Section 2 we give the equations governing vortex sheet separation and dynamics in notation similar to Jones [3]. In Section 3 we compute the flow for a benchmark problem—a half-period of sinusoidal oscillation of a plate—using the existing method of uniform smoothing on the free vortex sheets and zero smoothing on the plate. In Section 4 we pose a model problem which shows clearly the convergence rates with respect to δ in different important quantities both near and far from the plate edge. We study the model problem with the previous method, which we call “standard smoothing,” and with the new methods, which we call “velocity smoothing” and “tapered smoothing.” The velocity smoothing method uses smoothing only for computing the velocity of the free vortex sheet. The tapered smoothing method uses smoothing which tapers to zero at the plate edge. We identify the convergence rates for all methods with respect to smoothing parameters, and criteria needed for relatively rapid convergence.

In Section 5 we formulate a simple velocity smoothing algorithm for unsteady problems, and test it on the oscillating plate problem. We find that errors tend to zero much more rapidly than in the standard smoothing method. In Section 6 we formulate a tapered smoothing algorithm for unsteady problems. The important features are: a new mesh for the free vortex sheet using a “mesh function,” a power-law interpolation of the free sheet vortex sheet shape near the plate edge, and a continual pruning of mesh points for computational efficiency. Here too, errors tend to zero rapidly, and good agreement is obtained with the results of the velocity smoothing method.

2. Creation and dynamics of vortex sheets

We consider the prescribed motion of a rigid flat plate started from rest in an inviscid fluid, as in [3]. The plate moves transversely to itself with sinusoidal oscillation, and has a position in the complex plane given by:

$$\zeta(s, t) = s - i \frac{KC}{\pi} \cos\left(\frac{\pi}{KC} t\right), \quad -1 \leq s \leq 1. \quad (1)$$

Here s is arc length along the plate. As time t increases from zero, the plate velocity increases linearly, and displacement increases quadratically, with time. The parameter KC , called the Keulegan–Carpenter number [19], is half the period of oscillation. For small viscosity (or, in dimensionless terms, large Reynolds number), a thin boundary layer forms on the plate, across which the component of fluid velocity tangent to the plate is brought sharply to zero on the plate [1]. Outside of the boundary layer, the flow is nearly irrotational. At the plate edges, the fluid in the boundary layer moves off of the plate into the outer flow, where it is called a free shear layer. In the limit that the Reynolds number becomes infinite, the boundary layer and free shear layers tend to lines of zero thickness, and are called bound and free vortex sheets, respectively [2]. A computed example of free vortex sheets are the dotted lines of Fig. 1, which emanate from the flat plate. The fluid velocity is discontinuous across a vortex sheet, but only in its component tangent to the sheet. The free vortex sheets emanate from each edge of the plate continuously in time. We represent the free vortex sheets and the body as a single complex contour $\zeta(s, t)$, with signed arc length s increasing from $s_{min}(t) \leq -1$ to -1 on the “minus” sheet, from -1 to 1 on the body, and from 1 to $s_{max}(t)$ on the “plus” sheet. The vortex sheet strength (equal to the local jump in tangential velocity) along the contour is denoted $\gamma(s, t)$. Here positive γ corresponds to counterclockwise fluid rotation. The cumulative circulation along the contour is defined as the integral of vorticity:

$$\Gamma(s, t) = \int_{s_{min}}^s \gamma(s', t) ds'. \quad (2)$$

By Kelvin’s Circulation Theorem, the circulation is conserved at fixed material elements of the free sheets [2]. Circulation thus serves as a Lagrangian marker for the free vortex sheets. Following [3] we define

$$\Gamma_+(t) = \Gamma(1, t) = - \int_1^{s_{max}} \gamma(s', t) ds', \quad (3)$$

$$\Gamma_-(t) = \Gamma(-1, t) = \int_{s_{min}}^{-1} \gamma(s', t) ds'. \quad (4)$$

Thus $\Gamma_+(t)$ is the negative of the total circulation in the plus sheet and $\Gamma_-(t)$ is the total circulation in the minus sheet. In (3) we have used the fact that the total circulation in the flow is zero at all times by Kelvin’s Circulation theorem, which requires the total circulation in the flow at any time to equal its initial value, which is zero for a flow started from rest [2].

The dynamics of the flow around a plate with prescribed motion may be summarized in three equations. The first equation is the kinematic condition, which states that the components of fluid velocity and plate velocity normal to the plate

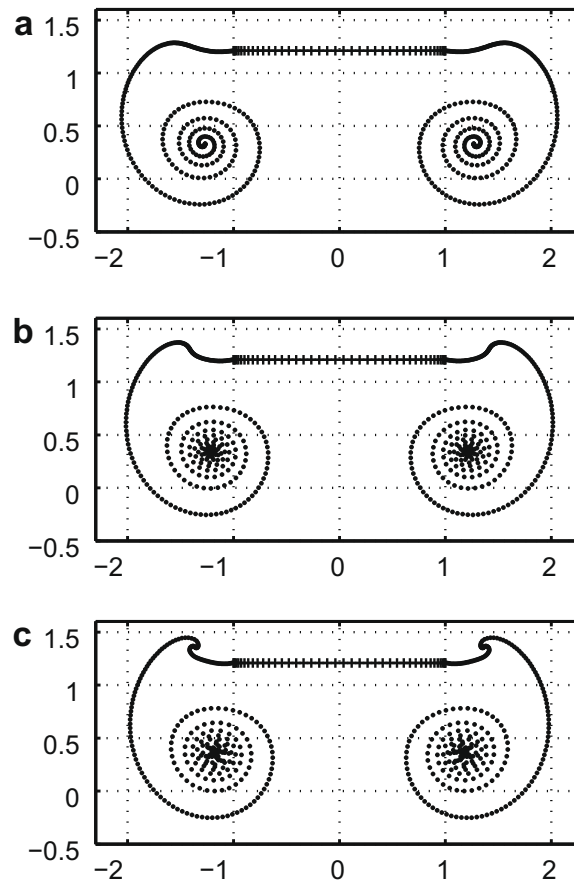


Fig. 1. The position of the plate and free vortex sheets at time $t = KC$, computed using standard smoothing with $\delta_0 = 0.2$ (a), 0.1 (b), 0.05 (c).

must match. In other words, fluid does not penetrate the plate. The second condition is the Kutta condition, which states that fluid velocity must be finite at the edges of the plate. The third equation is the Birkhoff–Rott equation, which gives the velocity of the vortex sheets. We now derive each of these equations, similarly to [3].

The complex-conjugate of the complex fluid velocity $u_x + iu_y$ induced at a point z by the bound and free vortex sheets is given by the Biot–Savart law for vortex sheets [1,2]:

$$u_x - iu_y|_z = \frac{1}{2\pi i} \int_{s_{\min}}^{s_{\max}} \frac{\gamma(s', t)}{z - \zeta(s', t)} ds'. \tag{5}$$

In the limit that z approaches a point $\zeta(s, t)$ on the rigid plate (Eq. (1)), the portion of the integral in Eq. (5) over the plate $-1 \leq s \leq 1$ is defined as a principal value integral:

$$u_x - iu_y|_{\zeta(s, t)} = \frac{1}{2\pi i} \int_{-1}^1 \frac{\gamma(s', t)}{s - s'} ds' + \frac{1}{2\pi i} \int_{s_{\min}}^{-1} \frac{\gamma(s', t)}{\zeta(s, t) - \zeta(s', t)} ds' + \frac{1}{2\pi i} \int_1^{s_{\max}} \frac{\gamma(s', t)}{\zeta(s, t) - \zeta(s', t)} ds', \quad -1 \leq s \leq 1. \tag{6}$$

$$= \frac{1}{2\pi i} \int_{-1}^1 \frac{\gamma(s', t)}{s - s'} ds' + \frac{1}{2\pi i} \int_0^{\Gamma_-(t)} \frac{d\Gamma'}{\zeta(s, t) - \zeta(\Gamma', t)} - \frac{1}{2\pi i} \int_0^{\Gamma_+(t)} \frac{d\Gamma'}{\zeta(s, t) - \zeta(\Gamma', t)}, \quad -1 \leq s \leq 1. \tag{7}$$

In Eq. (7), following [3], we have reparametrized the integrals over the free sheets by circulation, which is conserved in time on fluid particles comprising the free sheets. It is thus easy to keep track of $\Gamma(s, t)$ at all material points on the free sheets and obtain $\gamma(s, t)$ on the free sheets, when needed, as $\partial_s \Gamma(s, t)$.

The normal to the plate is in the $+y$ -direction. We denote the normal component of the plate velocity by $v(s, t)$, and set it equal to u_y in Eq. (7). After a minor rearrangement we obtain the kinematic condition:

$$\frac{1}{2\pi} \int_{-1}^1 \frac{\gamma(s', t)}{s - s'} ds' = f(s, t) = v(s, t) + \text{Re} \left[-\frac{1}{2\pi} \int_0^{\Gamma_-(t)} \frac{d\Gamma'}{\zeta(s, t) - \zeta(\Gamma', t)} + \frac{1}{2\pi} \int_0^{\Gamma_+(t)} \frac{d\Gamma'}{\zeta(s, t) - \zeta(\Gamma', t)} \right]. \tag{8}$$

For a known right hand side, Eq. (8) is a Cauchy singular integral equation to be solved for γ on the plate. A solution method convenient for computation is to expand the right hand side $f(s, t)$ as a Chebyshev series [20]:

$$f(s, t) = \sum_{k=0}^{\infty} f_k \cos(k\theta), \quad \theta = \arccos(s). \quad (9)$$

The solution to Eq. (8) is then

$$\gamma(s, t) = 2 \sum_{k=1}^{\infty} f_k \sin(k\theta) + \frac{-f_1 - 2f_0 \cos(\theta) + C}{\sin(\theta)}, \quad \theta = \arccos(s), \quad (10)$$

where C is an arbitrary constant. It is fixed by Kelvin's Circulation theorem, which requires the total circulation in the flow to be zero at all times. Thus

$$\int_{-1}^1 \gamma(s', t) ds' - \Gamma_+(t) + \Gamma_-(t) = 0. \quad (11)$$

With this constraint,

$$C = \frac{\Gamma_+(t) - \Gamma_-(t)}{\pi}. \quad (12)$$

The Kutta condition states that the velocity must be finite at the plate edges. Thus the jump in tangential velocity $\gamma(s, t)$ must be finite at $s = \pm 1$. Eq. (10) then implies that

$$-f_1 \pm 2f_0 + \frac{\Gamma_+(t) - \Gamma_-(t)}{\pi} = 0. \quad (13)$$

Eq. (13) is two equations for two unknowns, $\Gamma_{\pm}(t)$. With $\Gamma_{\pm}(t)$ thus chosen, the bound vorticity (Eq. (10)) becomes

$$\gamma(s, t) = 2 \sum_{k=1}^{\infty} f_k \sin(k\theta). \quad (14)$$

For the purpose of computation, it is convenient to analytically remove the logarithmic singularities of $f(s, t)$ in Eq. (6) at $s = \pm 1$, which cause slow ($\sim k^{-1}$) decay of the Chebyshev coefficients $\{f_k\}$. We thus write

$$f(s, t) = \tilde{f}(s, t) + \frac{1}{2\pi} \partial_s \Gamma(1, t) \log(1 - s) + \frac{1}{2\pi} \partial_s \Gamma(-1, t) \log(1 + s), \quad (15)$$

where $\tilde{f}(s, t)$ is a bounded continuous function. Therefore its Chebyshev coefficients, $\{\tilde{f}_k\}$, decay faster than those of f . In terms of $\{\tilde{f}_k\}$ the Kutta conditions (Eq. (13)) become

$$-\tilde{f}_1 \pm 2\tilde{f}_0 - \frac{1}{\pi} \partial_s \Gamma(1, t) (1 \mp \log(2)) + \frac{1}{\pi} \partial_s \Gamma(-1, t) (-1 \mp \log(2)) + \frac{\Gamma_+(t) - \Gamma_-(t)}{\pi} = 0. \quad (16)$$

Also, the solution γ (Eq. (14)) becomes

$$\gamma(s, t) = 2 \sum_{k=1}^{\infty} \tilde{f}_k \sin(k\theta) + \frac{1}{\pi} \partial_s \Gamma(1, t) (\pi - \theta) + \frac{1}{\pi} \partial_s \Gamma(-1, t) \theta. \quad (17)$$

Continuity of γ from the body to the vortex sheets may be seen by inserting $\theta = 0$ and π into Eq. (17).

Having solved for the strength of bound vorticity and the circulation in the free sheets at each time, we may apply Eq. (6) on the free sheets to obtain the Birkhoff–Rott equation for the motion of the free sheets. A point $\zeta(\Gamma, t)$ on the plus free sheet, for example, moves with the local fluid velocity given by the limit of Eq. (6) on the plus sheet which again becomes a principal value integral, similar to that in Eq. (7):

$$\partial_t \bar{\zeta}(\Gamma, t) = \frac{1}{2\pi i} \int_{-1}^1 \frac{\gamma(s', t)}{\zeta(\Gamma, t) - \zeta(s', t)} ds' + \frac{1}{2\pi i} \int_0^{\Gamma_-(t)} \frac{d\Gamma'}{\zeta(\Gamma, t) - \zeta(\Gamma', t)} - \frac{1}{2\pi i} \int_0^{\Gamma_+(t)} \frac{d\Gamma'}{\zeta(\Gamma, t) - \zeta(\Gamma', t)}, \quad \Gamma \in [0, \Gamma_+(t)]. \quad (18)$$

For $\zeta(\Gamma, t)$ on the minus sheet, the principal value integral switches from the plus sheet to the minus sheet. Eqs. (16)–(18) represent a system of equations to be solved at each time t for $\gamma(s, t)$ on the plate, the total circulation in the free sheets, $\Gamma_{\pm}(t)$, and the positions of the free sheets (with \tilde{f} computed during the solution using Eqs. (8) and (15)).

3. Numerical method with uniform regularization

We first investigate a type of smoothing which has been employed in previous works [3,6,10–12] for simulating the separation of vortex sheets. After Rosenhead's early study [9], it was observed that simple discretizations of the principal value integral in the Birkhoff–Rott equation (18) can lead to chaotic motions as the mesh size is reduced. Krasny found that the chaotic motions are caused by the rapid growth of discretization errors [21], and used a simple regularized form of Eq. (6) to suppress the errors [4]:

$$\partial_t \bar{\zeta}(s, t) = \frac{1}{2\pi i} \int_{s_{\min}}^{s_{\max}} \gamma(s', t) \frac{\overline{\zeta(s, t) - \zeta(s', t)}}{|\zeta(s, t) - \zeta(s', t)|^2 + \delta_0^2} ds'. \quad (19)$$

Krasny found that the errors are suppressed when the uniform smoothing parameter δ_0 exceeds the smallest mesh spacing in the discretization of Eq. (19).

Jones used the same uniform regularization of the free sheets shed at the edges of the rigid plate [3]. However, no regularization was used for the bound vortex sheet in the kinematic condition (the left hand side of Eq. (8)), since such smoothing makes the equation ill-posed. The numerical effect of the ill-posedness may be seen by replacing the Cauchy kernel in Eq. (8) with the δ_0 -smoothed kernel in Eq. (19). Discretizing the modified version of integral equation (8) for γ , the smoothed kernel corresponds to a matrix with singular values which become arbitrarily small as the quadrature spacing decreases below δ_0 . With the bound vortex sheet unsmoothed, and the free sheets smoothed uniformly by δ_0 , Eq. (8) becomes

$$\frac{1}{2\pi} \int_{-1}^1 \frac{\gamma(s', t)}{s - s'} ds' = f(s, t) = v(s, t) + \text{Re} \left[-\frac{1}{2\pi} \int_0^{\Gamma_-(t)} \frac{\overline{\zeta(s, t) - \zeta(\Gamma', t)} d\Gamma'}{|\zeta(s, t) - \zeta(\Gamma', t)|^2 + \delta_0^2} + \frac{1}{2\pi} \int_0^{\Gamma_+(t)} \frac{\overline{\zeta(s, t) - \zeta(\Gamma', t)} d\Gamma'}{|\zeta(s, t) - \zeta(\Gamma', t)|^2 + \delta_0^2} \right] \quad (20)$$

and Eq. (18) becomes

$$\begin{aligned} \partial_t \bar{\zeta}(\Gamma, t) &= \frac{1}{2\pi i} \int_{-1}^1 \frac{\gamma(s', t)}{\zeta(\Gamma, t) - \zeta(s', t)} ds' + \frac{1}{2\pi i} \int_0^{\Gamma_-(t)} \frac{\overline{\zeta(\Gamma, t) - \zeta(\Gamma', t)}}{|\zeta(\Gamma, t) - \zeta(\Gamma', t)|^2 + \delta_0^2} d\Gamma' \\ &\quad - \frac{1}{2\pi i} \int_0^{\Gamma_+(t)} \frac{\overline{\zeta(\Gamma, t) - \zeta(\Gamma', t)}}{|\zeta(\Gamma, t) - \zeta(\Gamma', t)|^2 + \delta_0^2} d\Gamma', \quad \Gamma \in [0, \Gamma_+(t)]. \end{aligned} \quad (21)$$

The smoothing in Eq. (20) removes the logarithmic singularities at $s = \pm 1$ from f , so that its Chebyshev coefficients decay rapidly. The corresponding vorticity $\gamma(s, t)$ may then be represented accurately by a truncated version of the series in (14) with a modest number of modes (enough to resolve a length scale δ_0). We refer to methods which employ the type of smoothing in both of Eqs. (20) and (21), which is discontinuous across the plate edges, as “standard smoothing” methods, in order to distinguish them from the two new methods in this work.

3.1. Time-stepping

We simulate the flow when the plate moves sinusoidally as in Eq. (1) with $KC = 3.8$, an example studied by Jones [3]. Jones used an initial condition in which small point vortices are placed below the plate edges at the first time step. Here we adopt a similar initial condition, which uses a small initial segment of the vortex sheet as the initial condition.

Algorithm 1. Standard Smoothing

Initialization:

At time $t = 0$, the plus vortex sheet is initialized with a single point at $1 - i\frac{KC}{\pi}$, the $s = 1$ edge of the plate, and the minus vortex sheet is initialized with a single point at $-1 - i\frac{KC}{\pi}$, the $s = -1$ edge of the plate. Then the following iteration is performed to advance the flow:

For $k = 1, 2, \dots$:

- (1) The plate is moved to its new position at time $k\Delta t$ given by Eq. (1), and new points are added to each free vortex sheet at the new positions of the respective plate edges.
- (2) The circulation in each free sheet at these points is computed by solving the two Kutta conditions (13) explicitly for the two unknowns $\Gamma_+(k\Delta t)$ and $\Gamma_-(k\Delta t)$. The desingularized version (16) with \tilde{f} is not used here because the smoothing makes f in (20) bounded. To calculate the Chebyshev coefficients f_0 and f_1 , we discretize the δ_0 -smoothed integrals in Eq. (20) using the trapezoidal rule. The unknown total circulations $\Gamma_{\pm}(k\Delta t)$ appear linearly in these coefficients. Having solved the two-by-two linear system (13) for $\Gamma_{\pm}(k\Delta t)$, we assign these values of the circulation to the corresponding fluid material points at the plate edges.
- (3) Compute $f(s, k\Delta t)$ from (20) and $\gamma(s, k\Delta t)$ using Eq. (14).
- (4) Evolve the points composing the free vortex sheets forward in time. This is done by computing the velocity of each point at $t = k\Delta t$ from the δ_0 -smoothed version of the Birkhoff–Rott equation (21). The velocity is used to move points of the free sheet to their positions at the next time step $t = (k + 1)\Delta t$. The two newly-created points are moved with their velocity at $t = k\Delta t$, using a forward-Euler time discretization. The remaining points of the free sheet, having existed at previous times, are moved to their new positions using the second-order Adams–Bashforth scheme, using the values of velocity at $t = (k - 1)\Delta t$ and $k\Delta t$.

End

In Fig. 1, we give the position of the sheet computed at time $t = KC$, using $\Delta t = KC/300$. We use a Chebyshev–Lobatto discretization of the plate, convenient for obtaining Chebyshev coefficients from node values for f and γ :

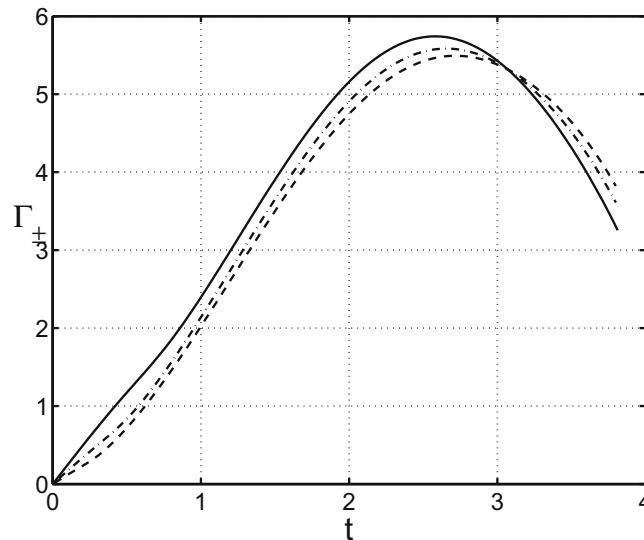


Fig. 2. The total circulation in each of the free sheets versus time, for uniform delta-smoothing on the free sheets and $\delta_0 = 0.2$ (solid line), 0.1 (dashed-dotted line), and 0.05 (dashed line).

$$s_j = \cos(j\pi/m), \quad j = 0, \dots, m. \tag{22}$$

We use $m = 41$ for the simulations in Fig. 1. We use three different values of δ_0 : 0.2 (a), 0.1 (b), and 0.05 (c). One can obtain a solution for arbitrarily small δ_0 by taking finer spacings of the free sheets (as found by [4]). Because the points on the free sheet are evolved with a first-order scheme for time Δt and with a second-order scheme for subsequent time, the scheme may be expected to have second-order convergence in Δt for $O(1)$ times. Numerical evidence of second-order temporal convergence of the scheme is presented in Appendix A. The convergence with respect to number of Chebyshev modes m is approximately third-order (due to the choice of quadrature rule for Eq. (20); see Fig. A.2(a)), though the decay of the Chebyshev modes $f_k, k = 1, \dots, m$ is exponential (see Fig. A.2(b)), as soon as m is large enough to resolve a length scale $O(\sqrt{\delta_0})$ near the plate ends. We shall explain the square-root behavior through a model problem in the next section. Due to the $O(m^{-2})$ density of Chebyshev–Lobatto points at the plate ends, resolution requires $m \gg \delta_0^{-1/4}$, which grows slowly as $\delta_0 \rightarrow 0$.

The convergence of solutions with respect to δ_0 is much slower than convergence with respect to m and Δt , and in some important quantities such as the velocity of the newly-created points of the free sheet near the plate edge, $O(1)$ errors remain as $\delta_0 \rightarrow 0$. The qualitative reason is that smoothing of vorticity occurs at the plate edges, where the solution is particularly sensitive to perturbations in the equations. The positions of the vortex sheet in the three panels of Fig. 1 are similar in many of the gross aspects but differ in some of the finer details. The positions of outermost turn of the spiral in the three panels of Fig. 1 are similar, with a slightly decreased width in panels c and b relative to a. The rolling-up of the next vortex spiral (above the plate in Fig. 1(c)) occurs with different timing and curvature in the three panels.

An important quantity is the total circulation in the free sheets as a function of time, plotted in Fig. 2. The three curves show a similar pattern of increase, local maximum, and decrease. The separation between the 0.05 and 0.1 lines is greater than half the difference between the 0.1 and 0.2 lines, indicating a convergence that is slower than first-order in δ_0 .

The numerical errors become particularly evident when we plot the vortex sheet strength γ at the instant $t = KC$, in Fig. 3. As noted in [3], the vorticity is discontinuous at the edges of the plate. Moving across the plate edge, the vorticity jumps from zero on the plate to an order-1 value on the free sheet. This jump in γ is a consequence of the jump in smoothing at the plate edges in Eq. (20). Furthermore, large differences are seen in the vorticity plot among the three values of δ_0 . This is due in part to the displaced timing of vortex shedding due to δ_0 evident in Figs. 1 and 2.

We now move from this particular example to a more general model problem, which will allow us to quantify precisely the inaccuracy due to smoothing, and consider how to reduce it. Smoothing is a limiting factor in both the accuracy and the computational cost of vortex-sheet-shedding computations. Because the maximum spacing between points on the free sheet for stable evolution scales with δ_0 as δ_0 tends to zero, the number of points needed to represent the free sheet grows as $1/\delta_0$ in this limit. Hence taking δ_0 to zero implies a large computational cost. We shall study this convergence rate and propose alternatives which give faster convergence with increased efficiency. In particular, we shall consider the possibility of making δ_0 smaller nearer the edge than farther away, with the intuition that the problem is dominated by the behavior of the flow near the edges of the plate.

4. A model problem

To study convergence in the limit $\delta_0 \rightarrow 0$, we formulate a quasistatic model problem. This avoids the expense of simulating unsteady free sheets with many mesh points, and more importantly, allows a more precise study of the asymptotic

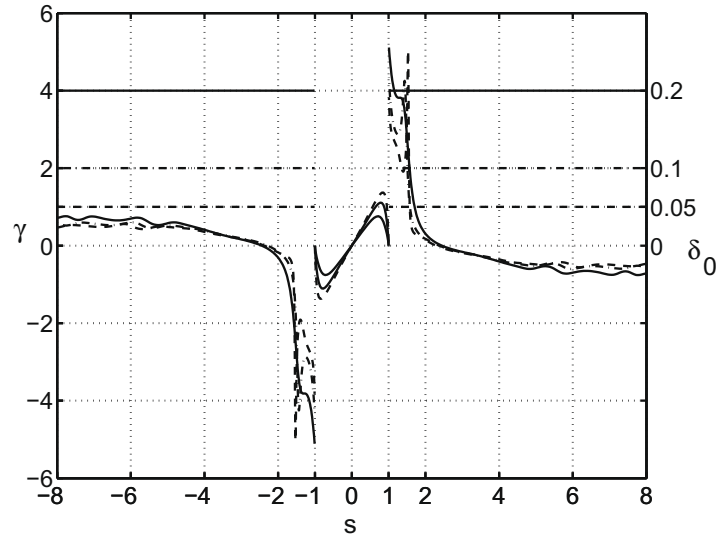


Fig. 3. The vortex sheet strengths versus arc length position on the body ($-1 < s < 1$) and the free sheets, for $\delta_0 = 0.2$ (solid line), 0.1 (dashed-dotted line), and 0.05 (dashed line).

behavior of numerical schemes as $\delta_0 \rightarrow 0$. The parameter δ_0 influences the problem in both the solution of the bound vorticity and shed vorticity—the smoothed kinematic condition (20) and the Kutta conditions (13)—and in the evolution of the free sheet—the smoothed Birkhoff–Rott equation (21). We solve for the bound and shed vorticity as before but assume a frozen, and simplified, geometry and distribution of vorticity on the free sheets. Instead of spirals with varying vorticity, we model the free sheets as straight line segments extending horizontally from the edges of the plate. We assume that the distribution of vorticity on the free sheets is uniform, but that its magnitude is set by the strength of shed vorticity.

With these assumptions Eq. (20) simplifies to:

$$\frac{1}{2\pi} \int_{-1}^1 \frac{\gamma(x')}{x-x'} dx' = f(x) = V_0 - \frac{1}{2\pi} \frac{\Gamma_0}{L-1} \int_{-L}^{-1} \frac{(x-x')}{(x-x')^2 + \delta_0^2} dx' + \frac{1}{2\pi} \frac{\Gamma_0}{L-1} \int_1^L \frac{x-x'}{(x-x')^2 + \delta_0^2} dx' \quad (23)$$

$$= V_0 + \frac{1}{4\pi} \frac{\Gamma_0}{L-1} \log \left(\frac{((x+1)^2 + \delta_0^2)((x-1)^2 + \delta_0^2)}{((x+L)^2 + \delta_0^2)((x-L)^2 + \delta_0^2)} \right). \quad (24)$$

Here the plus and minus free sheets occupy $1 < x < L$ and $-L < x < -1$, respectively. The plus/minus sheets have total circulation $\mp \Gamma_0$ and uniform vortex sheet strength $\mp \Gamma_0 / (L - 1)$, respectively.

By the symmetry of the problem under $x \rightarrow -x$, the Kutta condition (13) simplifies to

$$f_0 = \frac{1}{\pi} \int_{-1}^1 (1-x^2)^{-1/2} f(x) dx = 0. \quad (25)$$

Inserting f from (24) into (25) gives an equation which can be solved for Γ_0 . The resulting value is then used to compute $f(x)$ explicitly in Eq. (24). The bound vorticity γ is then given in terms of the Chebyshev coefficients of f by Eq. (14).

In Fig. 4(a) we plot the bound vorticity γ for $L = 4$ (with similar results for any value L such that $L - 1$ is of order one (in particular $L - 1 \gg \delta_0$)), $V_0 = 1$, and δ_0 ranging from 10^{-6} to 10^{-1} in half-decades. For $\delta_0 = 0$ we denote γ as $\bar{\gamma}$ and Γ_0 as $\bar{\Gamma}_0$. In Fig. 4(a), $\bar{\gamma}$ is the thick dotted line. It approaches its bounded values at the plate edges with a square-root behavior, which is implied by the desingularized form of the solution, Eq. (17). For all nonzero δ_0 , γ is zero at the edges, so there is an order-1 deviation there. The γ curves rise sharply to approach $\bar{\gamma}$, over a distance given by the x -distance between the peak of the δ_0 -smoothed γ curve and $x = -1$. These distances are plotted as triangles in Fig. 4(b), and scale as $\sqrt{\delta_0}$. The deviation $|\bar{\gamma} - \gamma|$ at a fixed value of $x = 1/\sqrt{2}$ for $\delta_0 > 0$ is given by the circles, and also scales as $\sqrt{\delta_0}$ for small δ_0 . The same scaling holds for the deviation at any fixed x , $-1 < x < 1$. Finally, the deviation in the total circulation $|\bar{\Gamma}_0 - \Gamma_0|/|\bar{\Gamma}_0|$ with respect to δ_0 is plotted as crosses. We again find a square-root behavior.

We briefly rationalize the $\sqrt{\delta_0}$ -convergence of γ and Γ_0 by considering the Chebyshev coefficients of γ in Eq. (14) expressed as weighted integrals of $f(x)$ in Eq. (24). The Kutta condition (25) and Eq. (24) imply that

$$\Gamma_0^{-1} = \frac{-V_0^{-1}}{4\pi^2(L-1)} \int_{-1}^1 (1-x^2)^{-1/2} \log \left(\frac{((x+1)^2 + \delta_0^2)((x-1)^2 + \delta_0^2)}{((x+L)^2 + \delta_0^2)((x-L)^2 + \delta_0^2)} \right) dx. \quad (26)$$

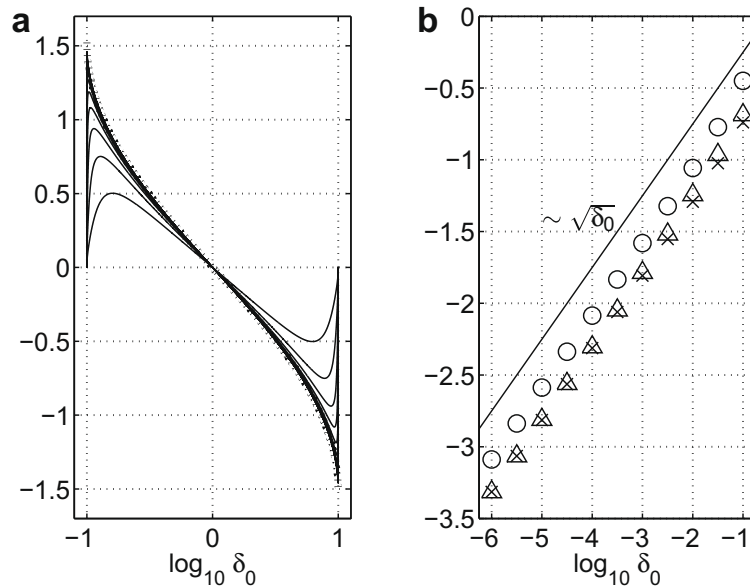


Fig. 4. (a) The bound vorticity γ for δ_0 ranging from 10^{-6} to 10^{-1} in half-decades (solid lines), and $\delta_0 = 0$ (dotted line). (b) For each curve in 'a' with $\delta_0 > 0$, the x -distance from the peak of γ to the $x = -1$ endpoint (triangles), the deviation $|\bar{\gamma} - \gamma|$ at $x = 1/\sqrt{2}$ (circles), and the deviation $|\bar{\Gamma}_0 - \Gamma_0|/|\bar{\Gamma}_0|$ (crosses). The solid line shows a square-root scaling with δ_0 .

Subtracting from Eq. (26) the same equation with $\delta_0 = 0$ we have

$$\bar{\Gamma}_0 - \Gamma_0 = \Gamma_0 \bar{\Gamma}_0 (\Gamma_0^{-1} - \bar{\Gamma}_0^{-1}) = \frac{-V_0^{-1} \Gamma_0 \bar{\Gamma}_0}{4\pi^2(L-1)} \times \int_{-1}^1 (1-x^2)^{-1/2} \log \left(\frac{(1 + (\delta_0/(x+1))^2)(1 + (\delta_0/(x-1))^2)}{(1 + (\delta_0/(x+L))^2)(1 + (\delta_0/(x-L))^2)} \right) dx. \quad (27)$$

Within δ_0 of an endpoint ($|x \pm 1| = O(\delta_0)$), the integrand is a product of $O(\delta_0^{-1/2})$ (the inverse square root term) and $O(1)$ (the log term) integrated over a region of length $O(\delta_0)$. The result is $O(\delta_0^{1/2})$, which is the size of the deviation in Γ_0 . For $|x \pm 1| = O(1)$, the integrand is a product of $O(1)$ (the inverse square root term) and $O(\delta_0)$ (the log term) integrated over a region of length $O(1)$, which is $O(\delta_0)$, subdominant to the near-endpoint contribution. The integral in (27) is thus $O(\delta_0^{1/2})$.

Deviations between γ and $\bar{\gamma}$ at $|x \pm 1| = O(1)$ can be described in terms of their Chebyshev coefficients. These can be expressed as integrals similar to that in Eq. (27), with the integrand now including the Chebyshev polynomial $T_k(x)$. The factor $T_k(x)$ does not change the scalings already noted for $\bar{\Gamma}_0 - \Gamma_0$. The $O(\delta_0^{1/2})$ scaling of the integral is maintained, and thus describes the deviation in a fixed Chebyshev coefficient (and thus the deviation in $\gamma(x)$ for fixed x) as $\delta_0 \rightarrow 0$.

The form of γ in Fig. 4(a) seems to agree well with the form of γ for $-1 < s < 1$ in the time-dependent simulations, exemplified by Fig. 3. Both show a sharp drop to zero in a region near the endpoints, which shrinks as $\delta_0 \rightarrow 0$. We note that in the time-dependent simulations, in the neighborhood of the edges the vortex sheets are straight and their strengths vary continuously from their values at the edges. Thus this model may be regarded as a leading-order approximation to the vortex sheet geometry and strength distribution in the neighborhood of the edges, where their influence on shedding is expected to be dominant. Furthermore, solving for Γ_0 for the whole sheet at once in the model problem approximates the accumulated effect of nonzero δ_0 on $\Gamma_{\pm}(t)$ during a time-dependent simulation.

We have addressed the convergence of γ and Γ_{\pm} with respect to δ_0 through the model problem. We now consider the convergence of flow velocities on the free sheet, as well as the shape of the free vortex sheet. In Fig. 5(a) we plot u_y at the plus sheet near the plate edge for δ_0 ranging from 10^{-4} to 10^{-1} in half-decades. The value of u_y for $\delta_0 = 0$ is denoted \bar{u}_y , and is the thick dashed line in Fig. 5(a). It tends to 1 like a square root as x decreases to 1 from above. Near the edge u_y for $\delta_0 > 0$ has a maximum which increases to 1.22 as $\delta_0 \rightarrow 0$. u_y changes continuously to its value of 1 on the plate, but with a diverging slope as $\delta_0 \rightarrow 0$. These maxima of u_y are plotted as circles in Fig. 5(b). Outside of a region of width $O(\delta_0)$ where velocity errors are $O(1)$, the curves converge to the unsmoothed solution like $\sqrt{\delta_0}$. The velocity deviation $|\bar{u}_y - u_y|$ at $x = 1.2$ is plotted versus δ_0 as crosses in Fig. 5(b). The solid line shows $\sqrt{\delta_0}$ scaling. Thus the error in the position of the vortex sheet for an unsteady simulation is expected to be dominated by an $O(\sqrt{\delta_0})$ error in velocity experienced over $O(1)$ time, leading to an $O(\sqrt{\delta_0})$ error in the position of the free vortex sheet.

We note that deviations in velocity tangent to the plate (i.e. u_x) are expected to be smaller than those normal to plate (i.e. u_y). For the model problem, the vortex sheets all lie on the x -axis, so the horizontal velocity u_x they induce at the x -axis is zero. For the benchmark unsteady problem in Section 2, the plate is horizontal but the free sheet is horizontal only at the plate edge. Farther away the free sheet is deflected from the horizontal, and it induces a tangential velocity at the plate edge which moves the vortex sheets off of the plate. This tangential velocity induced by far-field vorticity varies more smoothly near the plate edge than the locally-induced square-root behavior of the normal velocity shown by the dashed line in Fig. 5(a).

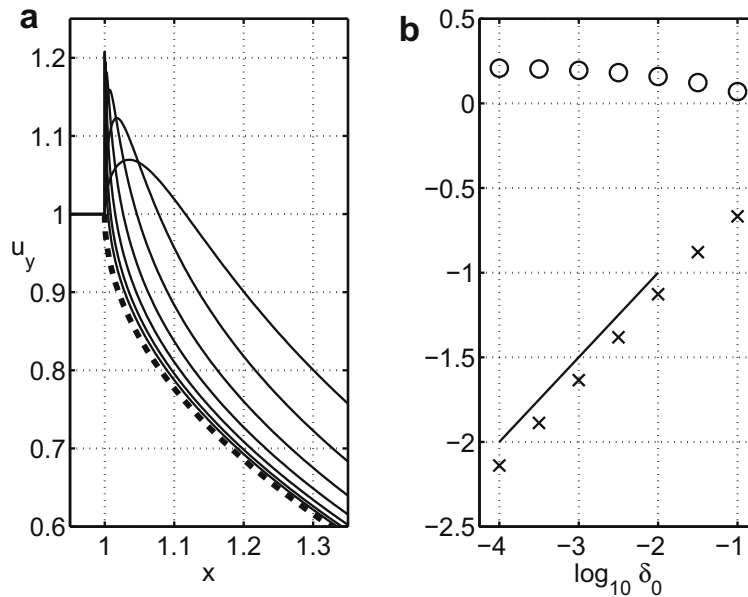


Fig. 5. (a) The vertical flow velocity $u_y(x)$ induced by the vortex sheets in the standard smoothing problem for $\delta_0 = 10^{-4}$ to 10^{-1} , increasing in half-decades (solid lines), and for $\delta_0 = 0$ (dashed line). (b) Maximum differences between $\delta_0 > 0$ and $\delta_0 = 0$ in u_y (circles) and difference at the fixed value $x = 1.2$ (crosses). The fitting line above the crosses shows the power-law $\delta_0^{-1/2}$.

4.1. Velocity smoothing

The model problem has quantified the error due to discontinuous vorticity smoothing at the plate edge in the solution of the kinematic equation (20). Vorticity smoothing is only needed, however, in the Birkhoff–Rott equation (21), to permit stable evolution of the free vortex sheet as studied by Krasny [4].

This suggests a simple alternative method: solve the kinematic equation and Kutta conditions (24) and (25) with $\delta_0 = 0$ to obtain the bound vorticity $\bar{\gamma}$ and shed circulation $\bar{\Gamma}_0$ with zero smoothing. Then compute the velocity induced by the bound and free vorticity along the plate and the free vortex sheet using a version of the Birkhoff–Rott equation (18) uniformly smoothed by δ_1 . The vertical velocity is then:

$$u_y(x) = \frac{1}{2\pi} \int_{-1}^1 \frac{\bar{\gamma}(x')(x-x')}{(x-x')^2 + \delta_1^2} dx' - \frac{1}{4\pi} \frac{\bar{\Gamma}_0}{L-1} \log \left(\frac{((x+1)^2 + \delta_1^2)((x-1)^2 + \delta_1^2)}{((x+L)^2 + \delta_1^2)((x-L)^2 + \delta_1^2)} \right). \quad (28)$$

The logarithmic terms come from the same integrals as in Eq. (24). Because the vorticity is continuous from the plate to the free sheet, and the free sheet vorticity is smoothed by δ_1 , the bound sheet vorticity must also be smoothed by δ_1 at the plate edge to avoid a logarithmic singularity there.

In Fig. 6(a) we plot u_y versus x near the right endpoint of the plate for $\delta_1 = 0$ and 10^{-4} up to 10^{-1} in quarter-decades. For $\delta_1 = 0$ we again obtain the unsmoothed solution \bar{u}_y (thick dashed line). The cases with $\delta_1 > 0$ are shown by the lower solid curves (for $x > 1$) and dashed curves (for $x < 1$). The lower solid curves approximate the upper solid curve well away from $x = 1$, but the deviation becomes larger near $x = 1$. The effect of $\delta_1 > 0$ is to smooth the square-root behavior of u_y at $x = 1$; the dashed lines show the smooth continuation of u_y into the region $x < 1$. These dashed values are not used in a time-dependent simulation, however; instead, the plate is evolved with its prescribed velocity which is 1 here. Thus, unlike the standard smoothing, velocity smoothing introduces a discontinuity in the normal velocity at the plate edge. Fig. 6(b) quantifies the behavior of the discontinuity $|u_y(1) - 1|$ as $\delta_1 \rightarrow 0$ (circles). The discontinuity tends to zero like $\sqrt{\delta_1}$, shown by the fit line. At a fixed location away from the edge $x = 1.000682$, we again measure the deviation in $u_y(x)$ between smoothed solutions and the unsmoothed solution (plotted as triangles). Here we find a transition from a $\sqrt{\delta_1}$ -convergence when $\delta_1 > 3 \times 10^{-3}$ to a δ_1^2 convergence when $\delta_1 < 3 \times 10^{-3}$, also shown by a fit line passing through the triangles at the smallest values. Hence much better accuracy is obtained more than a small distance from the plate edge. We can quantify the scaling of this small distance more precisely. For $\delta_1 > 0$, the slope of the velocity u'_y has a local minimum near the plate edge (unlike \bar{u}'_y , which diverges near $x = 1$). The position of this minimum quantifies the region of significant deviation from the unsmoothed curve. We plot the distance with crosses in Fig. 6(b) and find a good approximation to a linear behavior (shown with fit line). Therefore, while the maximum error decays slowly with δ_1 (as a square root), this error only persists over a range which tends to zero more rapidly—linearly with δ_1 .

The model problem indicates the error that can be expected in evolving the free sheets with a smoothed Birkhoff–Rott equation after the solution of γ and Γ_{\pm} without smoothing. The error is moderately large near the plate edges, but as points are advected away from the plate edge they soon reach a region of much smaller error. In an unsteady simulation, the value

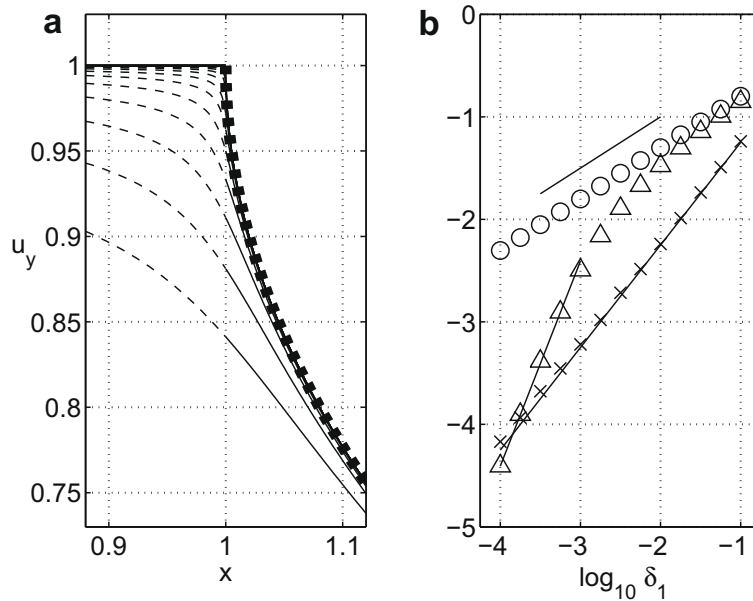


Fig. 6. (a) The vertical flow velocity $u_y(x)$ induced by the vortex sheets in the model problem for $\delta_1 = 0$ (topmost solid black line) and $\delta_1 = 10^{-4}$ to 10^{-1} , increasing in quarter-decades (dashed and solid lines below the topmost line). (b) Differences between $\delta_1 > 0$ and $\delta_1 = 0$ in terms of the value of u_y at the plate edge $x = 1$ (circles) and $x = 1.00086$ (triangles). The fitting line above the circle shows the power-law $\delta_1^{1/2}$, while that passing through the smaller values of the triangles shows δ_1^2 . The crosses measure the distance of local minima in slope du_y/dx from the edge $x = 1$, for $\delta_1 > 0$. This measures the extent of the region of $O(\sqrt{\delta_1})$ differences in panel a, as a function of δ_1 . The fit line through the crosses shows the scaling proportional to δ_1 .

of δ_1 should be at least the spacing between points near the plate edge, which is proportional to the time step Δt for a bounded velocity tangent to the plate edge. Therefore the error in velocity experienced by a Lagrangian point moving off of the plate edge is $O(\sqrt{\Delta t})$ for a duration of $O(\Delta t)$, and afterwards the error in velocity is $O(\delta_1^2) \sim O(\Delta t^2)$ (i.e., the scaling of the lower triangles in Fig. 6(b)). The error in the position of a point as it traverses the region of $O(\delta_1) = O(\Delta t)$ from the plate edge is the integral of the error in velocity over a time interval of $O(\Delta t)$, and is thus $O(\Delta t^{3/2})$. The error in position over the remainder of time is $O(\Delta t^2)$, so the total error is expected to be $O(\Delta t^{3/2})$. The solution of γ and Γ_{\pm} is exact up to the error in free sheet shape, so these quantities should also have errors of $O(\Delta t^{3/2})$. By contrast, for the standard smoothing method the model problem indicates $O(\Delta t^{1/2})$ convergence in vortex sheet shape.

4.2. Tapered smoothing

Smoothing only the velocity reduces the error significantly, but still includes error associated with smoothing of vorticity by a nonzero δ_1 at the plate edge. We now consider a method which uses zero smoothing at the plate edge. We assume that the smoothing parameter δ needs to be nonzero on the free sheet—larger than the spacing between mesh points—so that we may simulate the free vortex sheets with the widely-used regularization technique of Krasny [4]. We thus consider a non-uniform $\delta(x)$ which tends to zero as $x \rightarrow \pm 1$. Changing δ_0 to $\delta(x)$ in Eq. (23), we have

$$\frac{1}{2\pi} \int_{-1}^1 \frac{\gamma(x')}{x-x'} dx' = f(x) = V_0 - \frac{1}{2\pi} \frac{\Gamma_0}{L-1} \int_{-L}^{-1} \frac{(x-x')}{(x-x')^2 + \delta(x')^2} dx' + \frac{1}{2\pi} \frac{\Gamma_0}{L-1} \int_1^L \frac{x-x'}{(x-x')^2 + \delta(x')^2} dx'. \quad (29)$$

We now determine the behavior of $\delta(x)$ which is needed to obtain logarithmic singularities of equal strength on each side of Eq. (29) as $x \rightarrow \pm 1$. We hereafter assume that $\delta(x) = \delta(-x)$ and thus focus on behavior at the $x = 1$ edge only. When $x = 1$ and as $x' \rightarrow 1$, the kernels on the right hand side of Eq. (29) have the leading-order behavior

$$\frac{1-x'}{(1-x')^2 + \delta(x')^2} = \frac{1}{1-x'} - \frac{\delta^2(x')}{(1-x')^3} + \dots, \quad (30)$$

where we assume $\delta(x') < |1-x'|$ for the geometric series expansion on the right hand side to converge. For the second and subsequent terms in the series to be of lower order in $|1-x'|$ than the first, we require $\delta(x') \sim |1-x'|^p, p > 1$. For this range of p , the logarithmic singularities on each side of Eq. (29) at $x = 1$ cancel when γ is continuous there. The next order term on the right hand side of Eq. (30) is then integrable so there are no other singularities in Eq. (29).

We thus consider $\delta(x) \sim |1-x|^p, p > 1$ as $x \rightarrow 1$. We also wish for δ to approach a constant limiting value, δ_0 say, for larger x . The parameter δ_0 should be small enough for accuracy but large enough to allow for a moderately coarse mesh in the far field, limiting computational cost.

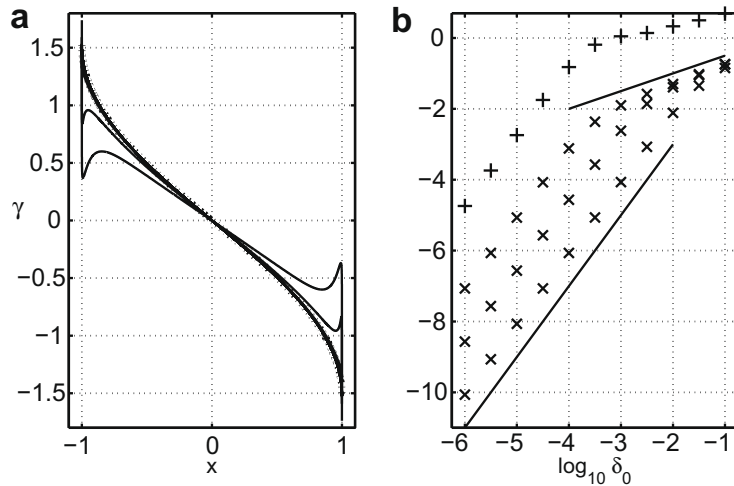


Fig. 7. For the model problem with nonuniform $\delta(x)$ (31): (a) with $\eta = 10^{-2}$, γ for δ ranging from 10^{-6} up to 10^{-1} in half-decades. The unsmoothed solution ($\delta_0 = 0$) is a thick dotted line. (b) Plusses give the maximum deviation in γ between smoothed and unsmoothed solutions shown in 'a,' where the maximum is taken over $-1 \leq x \leq 1$, $\eta = 10^{-2}$, and δ_0 is varied. The three lines of crosses give the relative deviation in Γ_0 between smoothed and unsmoothed solutions, for the three values of $\eta = 10^{-2}$ (bottom plot of crosses), 10^{-3} , and 10^{-4} (top plot of crosses).

We define a length η to quantify the transition in near-edge to far-from-edge behavior in $\delta(x)$. A possible choice for $\delta(x)$ is

$$\delta(x) = \delta_0 \frac{|(x-1)/\eta|^p}{1 + |(x-1)/\eta|^p}, \tag{31}$$

which approaches δ_0 for $|(x-1)| \gg \eta$. There are other possibilities for $\delta(x)$ satisfying the criteria mentioned so far. The form in (31) is convenient for defining a mesh of points in an unsteady simulation, as we shall show subsequently.

We now use the model problem to study the effect of a nonuniform $\delta(x)$ on the rate of convergence to the unsmoothed solution. In Fig. 7 we repeat the computation leading to Fig. 4 but with $\delta(x)$ as in (31). We use the exponent $p = 3/2$, but the results have the same asymptotic behaviors for all p bounded away from 1. As $p \rightarrow 1$ errors tend to the standard-smoothing behavior of Fig. 4 in asymptotic scaling but with different constant prefactors. In Fig. 7(a), we plot convergence of γ with $\eta = 10^{-2}$ and δ_0 again ranging from 10^{-6} up to 10^{-1} in half-decades. There are significant errors only for the two largest values of δ_0 , $10^{-1.5}$ and 10^{-1} , which are larger than η . Once δ_0 decreases below η , γ converges rapidly and uniformly to the solution of the unsmoothed problem (thick dashed line). In Fig. 7(b) we quantify convergence in terms of the maximum deviation in bound vorticity, $|\gamma - \bar{\gamma}|$, over $-1 \leq x \leq 1$ (plusses), and the relative deviation in total circulation $|\Gamma_0 - \bar{\Gamma}_0|/|\bar{\Gamma}_0|$ (crosses). For total circulation three lines are shown; the topmost corresponds to $\eta = 10^{-4}$ and the next two are for $\eta = 10^{-3}$ and 10^{-2} . We find that deviations in both quantities converge like $\sqrt{\delta_0}$, as in the standard smoothing case, for $\delta_0 > \eta$. As δ_0 decreases below η , there is a smooth transition to a much more rapid δ_0^2 -rate of convergence. The crossover in behavior when $\delta_0 \approx \eta$ is illustrated by the three lines of crosses.

In Fig. 8, we plot the vertical velocity near the plate for the tapered smoothing model, and find convergence behavior similar to that of γ . In Fig. 8(a), the vertical velocity again shows significant deviation only for the largest two values of δ_0 , $10^{-1.5}$

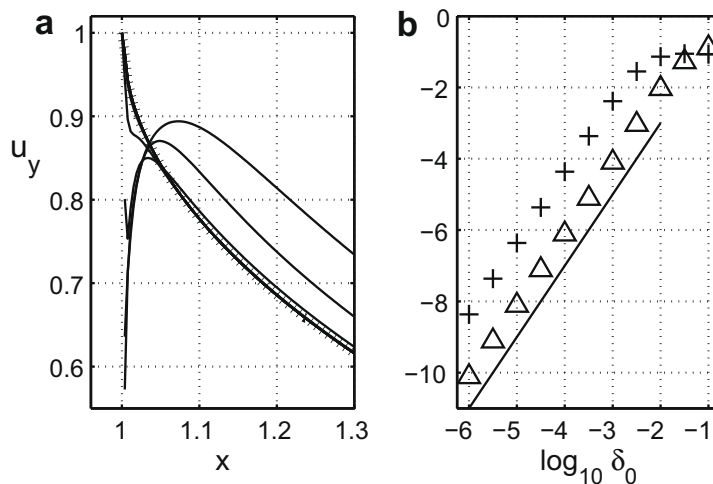


Fig. 8. For the model problem with variable delta (31): (a) with $\eta = 10^{-2}$, u_y for δ ranging from 10^{-6} up to 10^{-1} in half-decades. The unsmoothed solution ($\delta_0 = 0$) is a thick dashed line. (b) The deviation in γ between smoothed and unsmoothed solutions shown in 'a' at $x = 1.02$ (plusses) and $x = 1.2$ (triangles).

and 10^{-1} , which are larger than η . For $\delta_0 < \eta$ velocity converges uniformly to the unsmoothed solution like δ_0^2 . In Fig. 8(b) we plot the deviation at $x = 1.02$ (plusses) and $x = 1.2$ (triangles), and find δ_0^2 convergence once $\delta_0 < x - 1$.

These results show that for a given δ_0 , small ($O(\delta_0^2)$) errors can be achieved when $\delta(s)$ is brought to zero over a region η near the body edge which is somewhat larger than δ_0 . The $O(\delta_0^2)$ error can be attributed to the second term on the right hand side of Eq. (30), which gives the far-field error for a point vortex source smoothed by δ_0 . We have used the model problem to examine two new types of δ -smoothing in Sections 4.1 and 4.2. We now propose unsteady schemes based on these types of smoothing, with the goal of realizing the faster convergence we have found for the model problem.

5. A numerical method with velocity smoothing on the body

In Section 4.1 we examined the error due to velocity smoothing in the model problem. To formulate an efficient unsteady velocity smoothing algorithm, it is useful to combine velocity smoothing with the tapered smoothing of Section 4.2. More precisely, we use a nonuniform smoothing function which varies from a small nonzero constant $\delta_1 \sim O(\Delta t)$ at the plate edge to a larger constant δ_0 farther from the plate. The variation occurs over a distance $\eta > \delta_0$:

$$\delta_v(s) = \delta_1 + (\delta_0 - \delta_1) \frac{|(s-1)/\eta|^p}{1 + |(s-1)/\eta|^p}, \quad s \in (1, s_{max}] \tag{32}$$

$$= \delta_1, \quad s \in [-1, 1]. \tag{33}$$

$\delta_v(s)$ is extended to the minus sheet as an even function. The reason for using a tapered smoothing function instead of a uniform value of δ_1 is that it becomes expensive to resolve a vortex sheet for long times with a small smoothing parameter. The vortex sheet spirals develop more inner turns for smaller δ , and these turns require many points to resolve (see how the spirals in Fig. 1 vary with δ_0). The different spatial structure inside the spiral causes little change outside the spiral, where the flow is mainly influenced by the total circulation in the spiral. To avoid having to resolve the inner spiral structure far from the plate, we use a larger smoothing constant $\delta_0 \gg \delta_1$.

When the errors due to δ_0 and δ_1 are small, the total error can be expanded in a double asymptotic series of the parameters. The leading-order terms in the double series are the leading-order errors from each parameter separately; coupling terms involve higher-order products. In Section 4.1 we found that velocity smoothing by δ_1 causes velocity errors which are $O(\sqrt{\delta_1})$ in a region extending a distance of $O(\delta_1)$ from the body, and velocity errors which are $O(\delta_1^2)$ beyond this region. In Section 4.2 we found that tapered smoothing causes errors in both the vorticity and velocity which are uniformly $O(\delta_0^2)$ once the tapering distance η exceeds δ_0 .

The model problem indicates the error that can be expected in using a Birkhoff–Rott equation smoothed after the solution of γ and Γ_{\pm} without smoothing. The error is moderately large near the plate edges, but as points are advected away from the plate edge they rapidly reach a region of much smaller error. The value of δ_1 is chosen to be a multiple of the spacing between points near the plate edge, which is proportional to the time step Δt for a given velocity tangent to the plate edge. Therefore the error in velocity experienced by a Lagrangian point is $O(\sqrt{\Delta t})$ for a duration of $O(\Delta t)$, and afterwards the error in velocity is $O(\Delta t^2)$. The error in position of a point as it traverses the region of $O(\delta_1) = O(\Delta t)$ from the plate edge is the integral of the error in velocity over a time interval of $O(\Delta t)$, and is thus $O(\Delta t^{3/2})$. The error in position over the remainder of time is $O(\Delta t^2)$. Hence the leading-order terms in the error are $\sim \Delta t^{3/2} \sim \delta_1^{3/2}$ and $\sim \delta_0^2$.

We can state the velocity smoothing algorithm in terms of its differences from the standard smoothing algorithm of Section 3. We replace (20) with the unsmoothed kinematic equations (8) and (21) with the velocity-smoothed version

$$\begin{aligned} \partial_t \bar{\zeta}(s, t) = & \frac{1}{2\pi i} \int_{-1}^1 \frac{\gamma(s', t)(s-s')}{(s-s')^2 + \delta_1^2} ds' + \frac{1}{2\pi i} \int_0^{\Gamma_-(t)} \frac{\bar{\zeta}(s, t) - \zeta(\Gamma', t)}{|\zeta(s, t) - \zeta(\Gamma', t)|^2 + \delta_v(\Gamma')^2} d\Gamma' \\ & - \frac{1}{2\pi i} \int_0^{\Gamma_+(t)} \frac{\bar{\zeta}(s, t) - \zeta(\Gamma', t)}{|\zeta(s, t) - \zeta(\Gamma', t)|^2 + \delta_v(\Gamma')^2} d\Gamma', \quad s \in [s_{min}, -1) \cup (1, s_{max}]. \end{aligned} \tag{34}$$

Algorithm 2. Velocity Smoothing

Initialization: Same as Algorithm 1.

For $k = 1, 2, \dots$:

(1) Same as Algorithm 1.

(2) The circulation in each free sheet at the new edge points is computed by solving the two Kutta conditions (13) implicitly for the two unknowns $\Gamma_+(k\Delta t)$ and $\Gamma_-(k\Delta t)$. The desingularized version (16) is used. To calculate the Chebyshev coefficients \tilde{f}_0 and \tilde{f}_1 , we require initial guesses for the unknown total circulations in the free sheets at the current time step $\Gamma_{\pm}(k\Delta t)$. These guesses are used to form the $\partial_s \Gamma$ terms in Eq. (15), which are needed to desingularize f in Eq. (8). We iterate using Broyden's method [22] until we have $\Gamma_{\pm}(k\Delta t)$ which satisfy the Kutta condition (16) with a small tolerance 10^{-12} . Usually only 2–3 iterations are required to solve the 2-by-2 linear system since a very good initial guess can be extrapolated from previous time steps. Having solved for $\Gamma_{\pm}(k\Delta t)$, we assign these values of the circulation to the corresponding fluid material points at the plate edges.

- (3) Compute $\tilde{f}(s, k\Delta t)$ from (15) using $\partial_s \Gamma$ -terms computed with correct values of $\Gamma_{\pm}(k\Delta t)$ from step 2. Compute $\gamma(s, k\Delta t)$ using Eq. (17).
- (4) Evolve the points composing the free vortex sheets forward in time as in Algorithm 1 but using the δ_v -smoothed version of the Birkhoff–Rott equation (34).

End

We solve the test problem of Section 2 using uniform time-stepping with $\Delta t = KC/600$. We choose $\delta_1 = 0.01$, which the time step (and thus the spacing between points near the plate edge) is small enough to permit. We use $\delta_0 = 0.2$, and $m = 141$. The value of m is chosen so that there are several points on the plate which are closer to the edge than the nearest point from the vortex sheet. This ensures that the solution for γ on the body is well-resolved.

The results for the oscillating plate are shown in Fig. 9. In Fig. 9(a), the shape of the vortex sheet is similar to that in Fig. 1(c), which used a uniform $\delta_0 = 0.05$. The vortices which are beginning to form in Fig. 9(a) are somewhat tighter spirals. Also, the vortex sheet is curved more sharply at the plate edge, and does not extend as far from the plate in the horizontal or vertical directions. In Fig. 9(b) we plot the distribution of γ versus s , which is dramatically different from the plots in Fig. 3. The sharp spike in vorticity at the plate edges is resolved here because the spacing of points on the free sheet and plate near the plate edge is less than 10^{-3} , which is smaller than the spike width, which is larger than 10^{-2} . Fig. 9(c) shows the values of $\delta_v(s)$ (plusses) near the $s = 1$ edge, together with the spacing between points on the free-sheet mesh (crosses). It may be seen that a value significantly smaller than $\delta_1 = 0.01$ could cause problems in the stability of the vortex sheet dynamics for this time step. Fig. 9(d) shows the time-evolution of total circulation in the minus sheet for velocity smoothing (lower solid line) compared with the three lines of Fig. 2. The curves are qualitatively similar but the difference between the current curve and those for uniform δ_0 is significant. We recall that for the model problem, the convergence with uniform δ_0 occurs at a rate $\sim \sqrt{\delta_0}$.

In Table 1, in the first five rows, we list the maximum circulation shed for five different time steps, decreasing by a factor of 2. Smaller Δt permits smaller δ_1 , in proportion to Δt . The relative deviations between the values of Γ^v (denoting circulation for the velocity smoothing algorithm) in the first four rows decrease by a factors of approximately four with each halving of the time step. At $\Delta t = 2KC/600$ and below, the relative error stagnates at about 10^{-3} . The cause appears to be the error in approximating the initial spiral-vortices by line segments, together with the impulsive acceleration at $t = 0$. The last four rows of the table show the effect of varying δ_0 , with $\eta = 2\delta_0$. In the velocity smoothing method the relative error again stagnates at about 10^{-3} once δ_0 reaches 0.1. For comparison the results of the standard smoothing method (denoted $|\Gamma^s|$) are shown in the last column. The values are well fit by a line of form $|\Gamma^s| = C\sqrt{\delta_0}$ which reaches $|\Gamma^s| = 5.3$ at $\delta_0 = 0$.

A consequence of using smoothing only for the Birkhoff–Rott equation is that the integrals over the free sheets must be computed twice per time step: once for Eq. (8) and once for Eq. (34). The work can be reduced to nearly that of a single computation by using the same smoothed kernel for the free sheets at a sufficient distance from the plate edge. Another consequence of using smoothing only for the Birkhoff–Rott equation is that it introduces error into the no-penetration condition on the plate. We note, however, that such error already exists in the standard smoothing algorithm, because of the discrete plate mesh. The no-penetration error due to the discrete plate mesh becomes significant when the free sheet becomes nearer

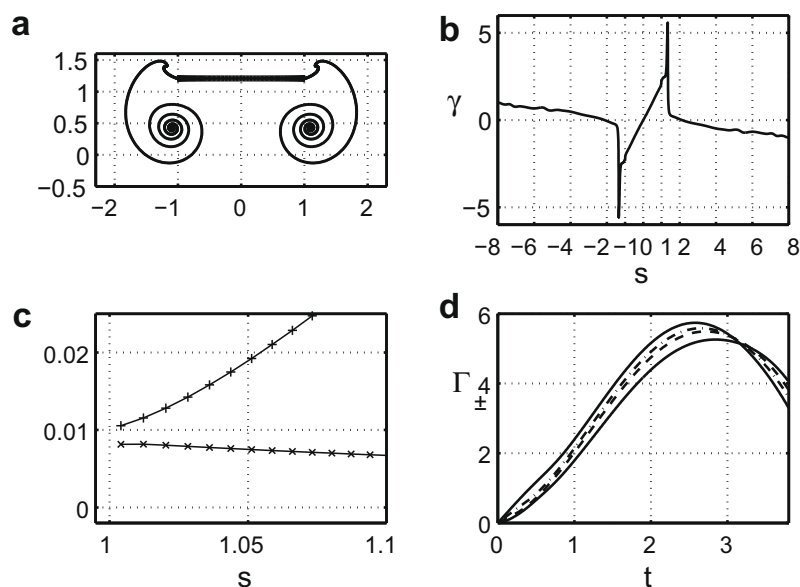


Fig. 9. (a) The position of the plate and free vortex sheets at time $t = KC$. (b) The distribution of γ versus s at time $t = KC$. (c) The vortex sheet smoothing parameter $\delta_v(s)$ (plusses) and the spacing between points (crosses) plotted versus arc length s near one edge of the plate. (d) The total circulation versus time for the uniform-delta cases of Fig. 2 (three upper lines), and the velocity-smoothed case (lower solid line).

Table 1

Maximum circulation in the velocity smoothing method ($|I^v(t)|$) and standard smoothing method ($|I^s(t)|$) for the benchmark problem of Section 2.

Δt	δ_1	δ_0	$\text{Max} I^v(t) $	$\text{Max} I^s(t) $
16KC/600	1.6 Δt	0.2	5.1016	–
8KC/600	1.6 Δt	0.2	5.2474	–
4KC/600	1.6 Δt	0.2	5.2746	–
2KC/600	1.6 Δt	0.2	5.2692	–
KC/600	1.6 Δt	0.2	5.2614	–
2KC/600	1.6 Δt	0.2	5.2692	5.7432
2KC/600	1.6 Δt	0.1	5.3061	5.5859
2KC/600	1.6 Δt	0.05	5.3075	5.4940
2KC/600	1.6 Δt	0.025	5.2939	5.4337

to the plate than the mesh spacing. By confining the region of δ_1 -smoothing on the plate to a distance of $O(\delta_1)$ from the plate edges, the no-penetration error due to velocity smoothing can be reduced significantly relative to that from the discrete plate mesh. We now discuss the tapered smoothing algorithm, which does not introduce error into the no-penetration condition.

6. A numerical method with tapered regularization

In Section 4.2 we solved the model problem with tapered smoothing, which avoids the nonzero smoothing at the plate edge present in the velocity smoothing method. We now propose an algorithm for unsteady simulations with zero smoothing at the plate edge. When evolving the free vortex sheets, we must take care that the spacing between mesh points remains smaller than the local value of the smoothing function.

In Section 3, where δ is uniform, a single new point was inserted into the free sheet at the plate edge at each time step. If the spacing between points becomes larger than δ_0 , numerical instability may occur. The spacing between points is a product of the time step Δt with the flow speed tangent to the plate $\mu(s, t)$ evaluated at the edges $s = \pm 1$. Hence we obtain a constraint $\Delta t < \delta_0 / \mu(\pm 1, t)$. This constraint is usually not very severe for δ_0 ranging from 0.05 to 0.2 as in Section 3 and previous works [3,10], since $\mu(\pm 1, t)$ is typically close to 1 in order of magnitude for an oscillatory flow nondimensionalized on plate length and oscillation period as in Section 3.

The model problem with nonuniform $\delta(s)$ has shown that relatively fast ($O(\delta_0^2)$) and uniform convergence of γ can be obtained when $\delta(s)$ tends to zero faster than $|1 - s|$ as s approaches 1. Since the spacing between points should be smaller than $\delta(s)$, the spacing between mesh points should also tend to zero faster than $|1 - s|$, which is also their distance from the plate edge, along the free sheet. In this case it is not sufficient to insert a single new point into the free sheet at the plate edge at each time step as in Section 3. If the tangential flow speed $\mu(1, t)$ is nearly constant in time, the points will be nearly uniformly spaced, so their spacing will tend to zero like $|1 - s|$ as s approaches 1. This convergence is too slow to be bounded by a $\delta(s) \sim |1 - s|^p$, $p > 1$. If the tangential flow speed $\mu(1, t)$ increases in time, the spacing between points will increase approaching the plate edge, which is even worse.

Our modification for nonuniform $\delta(s)$ is to insert multiple new points into the free sheet with each time step so as to guarantee a mesh spacing smaller than $\delta(s)$ over a region of the free sheet which can be made arbitrarily close to the plate edge. We thus avoid numerical instabilities due to insufficient spacing. An additional benefit of this approach is that we obtain higher resolution nearer the plate edge than farther away. Since the flow is expected to exhibit sharper gradients near the plate edges, this is a more efficient apportionment of mesh resolution than is a uniform mesh.

We again consider the smoothing function (31) from Section 4.2, but which is now a function of arc length s :

$$\delta_t(s) = \delta_0 \frac{|(s - 1)/\eta|^p}{1 + |(s - 1)/\eta|^p}. \tag{35}$$

We first determine a mesh which has a spacing smaller than $\delta_t(s)$ given in (35). To avoid numerical instability, our mesh must have at most this (nonuniform) spacing between points.

6.1. Mesh function

We define a mesh function $s(k)$ which maps points indexed by positive integers k onto free sheet positions with arc length s . We find $s(k)$ by solving a differential equation which approximates the condition that the spacing between adjacent points is a fixed fraction c_2 of $\delta_t(s)$:

$$\frac{ds}{dk} = c_2 \delta_t(s). \tag{36}$$

Using $\delta_t(s)$ given in Eq. (35), Eq. (36) may be integrated to yield

$$\frac{\eta}{c_2 \delta_0} \left(\frac{s-1}{\eta} + \frac{1}{1-p} \left(\frac{s-1}{\eta} \right)^{1-p} \right) = k + c. \tag{37}$$

The constant c is fixed by specifying that the first point $k = 1$ lies at a known arc length from the plate edge. For the choices $p=3/2$ or 2 , Eq. (37) may be solved explicitly for s by solving a cubic or quadratic equation. As k increases, the mesh points approach the plate edge with increasing density (which is necessary since $\delta_t(s)$ tends to 0). Using Eq. (37) we find that for large k , the location of the points and the spacing between neighbors scale as

$$(s - 1) \sim k^{1/(1-p)}, \tag{38}$$

$$\delta(s) \sim (s - 1)^p \sim k^{p/(1-p)}. \tag{39}$$

For $p = 2, \frac{3}{2}, \frac{4}{3}, \dots, \frac{n+1}{n}, \dots$, these values are

$$(s - 1) \sim k^{-n}, \tag{40}$$

$$\delta(s) \sim (s - 1)^p \sim k^{-(n+1)}. \tag{41}$$

As the exponent p decreases towards 1, n increases. Thus the free sheet mesh points tend to the plate edge more rapidly. Thus it is possible to represent the part of the free sheet up to a given distance from the plate edge with fewer points. However, the function $\delta_t(s)$ becomes less smooth at $s = 1$ as p decreases towards 1. In particular, the second derivative is singular for $p < 2$, and the first derivative approaches a jump as p tends to 1.

With only a finite number of points in the mesh, there is a gap from the last mesh point to the plate edge. The last mesh point has $k = k_{max}$ and distance from the plate edge $\sim k_{max}^{-n}$ (from (40)). The spacing between the last two mesh points is $\sim k_{max}^{-(n+1)} \ll k_{max}^{-n}$ (from (41)). Thus at the last mesh point, there is an abrupt change in mesh spacing, from $\sim k_{max}^{-(n+1)}$ to a much larger value $\sim k_{max}^{-n} \gg \delta(s)$. This change leads to inaccuracy when computing the velocity of the last mesh point and nearby points using the discretized Birkhoff–Rott equation.

One way to remedy this is to extend the mesh into the gap, with uniform spacing equal to the spacing between the last two points of the mesh function. As these new “gap points” approach the plate edge, the local value of $\delta_t(s)$ falls below the uniform mesh spacing, so these points may not be evolved forward in time stably using the smoothed Birkhoff–Rott equation. However, they may still be used as source points of vorticity for the tapered-smoothing kinematic equation:

$$\frac{1}{2\pi} \int_{-1}^1 \frac{\gamma(s', t)}{s - s'} ds' = f(s, t) = v(s, t) + \text{Re} \left[-\frac{1}{2\pi} \int_0^{\Gamma_-(t)} \frac{\overline{\zeta(s, t) - \zeta(\Gamma', t)} d\Gamma'}{|\zeta(s, t) - \zeta(\Gamma', t)|^2 + \delta_t(\Gamma')^2} + \frac{1}{2\pi} \int_0^{\Gamma_+(t)} \frac{\overline{\zeta(s, t) - \zeta(\Gamma', t)} d\Gamma'}{|\zeta(s, t) - \zeta(\Gamma', t)|^2 + \delta_t(\Gamma')^2} \right] \tag{42}$$

and the tapered-smoothing Birkhoff–Rott equation:

$$\begin{aligned} \partial_t \bar{\zeta}(s, t) = & \frac{1}{2\pi i} \int_{-1}^1 \frac{\gamma(s', t)}{s - s'} ds' + \frac{1}{2\pi i} \int_0^{\Gamma_-(t)} \frac{\overline{\zeta(s, t) - \zeta(\Gamma', t)}}{|\zeta(s, t) - \zeta(\Gamma', t)|^2 + \delta_t(\Gamma')^2} d\Gamma' \\ & - \frac{1}{2\pi i} \int_0^{\Gamma_+(t)} \frac{\overline{\zeta(s, t) - \zeta(\Gamma', t)}}{|\zeta(s, t) - \zeta(\Gamma', t)|^2 + \delta_t(\Gamma')^2} d\Gamma', \quad s \in [s_{min}, -1) \cup (1, s_{max}]. \end{aligned} \tag{43}$$

We use the gap points in computing the integrals on the right hand side of Eqs. (42) and (43). The integrand then varies smoothly over the quadrature points when the target points on the left hand side are the last several mesh function points. We evolve the mesh function points forward (stably) using Eq. (43), but do not evolve the gap points forward.

6.2. Time-stepping

Having defined a mesh which meets the spacing requirements for stable evolution of the free vortex sheets, we now describe how the mesh is used in an unsteady algorithm. At each time step, we advance the free sheets and plate in an alternating fashion as before. Each time we advance the plate, we interpolate to find the shape of the free sheet between the plate edges and the previously-advanced free sheet. On the first time step, the shape is assumed to be a small semicircle (an approximation to the outer turn of a spiral). On subsequent steps, the shape is assumed to be a power-law function of form

$$y - y(\pm 1) \sim C(x - x(\pm 1))^\alpha \tag{44}$$

near the plate edges $s = \pm 1$. We know the plate edge position $x(\pm 1) + iy(\pm 1)$ and use the slopes at the plate edge and the end of the previously-advanced free sheet to determine C and α . A power-law fit is appropriate because the normal velocity has a square-root behavior near the plate edge (Fig. 6(a)), so the position will also have a power-law behavior for a smooth tangential velocity near the plate edges.

For computational efficiency it is useful to eliminate points when the mesh spacing is much finer than $\delta_t(s)$. This occurs as the high-density mesh near the plate edge is advected away from the plate, where $\delta_t(s)$ is larger. At each time step we check

the spacing between the two nearest neighbors of every other point in the free sheet after advancing it forward with the Birkhoff–Rott equation. If we find that the spacing is smaller than

$$c_3 \delta_t(s), \quad (45)$$

where c_3 is a small fraction (here we use $1/5$), the central point may be safely eliminated and the density will be sufficiently high for stable and accurate evolution. We repeat this check until no more points can be removed, and then proceed to solve the kinematic condition and Kutta condition with the remaining free sheet points and their circulations. Since the cost of computing nearest-neighbor distances is linear in the number of free sheet points, the cost of removing points is insignificant compared to the evaluation of the Birkhoff–Rott equation (which is quadratic in the number of free sheet points).

Algorithm 3. Tapered Smoothing

Initialization: Same as Algorithm 1.

For $k = 1, 2, \dots$:

- (1) The plate is moved to its new position at time $k\Delta t$ given by Eq. (1). An interpolated sheet shape is fit to the interval between the existing free sheet and the plate edges using Eq. (44). Mesh function points are added to a fraction c_4 of the total arc length of the interpolated sheet shape starting from the existing free sheet using the mesh function (37). Gap points are used to fill the remaining portion of the interpolated sheet shape as described in Section 6.1. The constant c in (37) is fixed by setting the first point $k = 1$ to lie at the last point of the existing free sheet.
 - (a) Remove superfluous points according to (45).
- (2) Same as Algorithm 2, but using Eq. (42) in place of Eq. (8). Also, monotonic cubic Hermite interpolation is used to obtain the values of Γ at new points in the interpolated interval created in step 1, using the values of Γ at previously existing free sheet points and at the plate edge.
- (3) Same as Algorithm 2, but using Eq. (42) in place of Eq. (8). Γ is interpolated at new points in the interpolated interval as in step 2.
- (4) Evolve the mesh function points but not the gap points forward in time as in Algorithm 1 but using the δ_t -smoothed version of the Birkhoff–Rott equation (43), as described in Section 6.1.

End

The choice of the fraction c_4 in step 1 merits further discussion. In principle we would like to add mesh function points as close to the plate edge as possible. However, we recall that the velocity has a square-root behavior at the plate edge (Fig. 6(a)). Hence the multistep schemes we use here (Forward Euler and Two-step Adams Bashforth) will only give accurate results if the points travel a small distance relative to their distance from the plate edge. Then the points will be sufficiently far from the square root velocity singularity so that the local Taylor expansion of the velocity used in multistep schemes is accurate over the distance traveled by the points. In the results to be presented we set $c_4 = 1/6$, so new mesh function points fill $1/6$ of the interpolated sheet shape and gap points fill the remaining $5/6$. Mesh function points travel only about $1/6$ as far as their distance from the plate edge on the first time step. On subsequent time steps the points are farther from the singularity so the multistep schemes are sufficiently accurate for all points for which they are used.

One alternative approach to evolving points near the square-root velocity singularity is to estimate the square-root behavior of velocity at each time step and correct the motion of the points accordingly. Another possibility is to switch from a Lagrangian to an Eulerian representation of the vortex sheet near the plate edge. At a fixed arc length distance s from the edge, velocities vary more smoothly in time than for a fixed material point, so conventional time-stepping methods can be applied for the Eulerian velocity of the curve, which is its velocity normal to itself. This approach introduces new issues associated with updating the circulation in the Eulerian coordinate, where it is no longer conserved in time, and introduces new sources of instability in coupling the motion of the vortex sheet to its shape through the local normal vector. We have not been able to find a reasonably simple way to implement either of these alternatives thus far.

We now give the result of the tapered smoothing method for the oscillating plate problem considered in Section 2. In practice, we use the velocity smoothing method (Algorithm 2) for the first several time steps and then switch to Algorithm 3. This start-up phase is needed to generate 1–1.5 complete turns of the vortex spiral which is the asymptotic early time solution obtained by Pullin [23]. Otherwise, seemingly small deviations from the correct spiral solution lead to instability in the early evolution of the vortex sheet under Algorithm 3, partly due to the sheet interpolation near the plate edge in step 1. There is a sensitive coupling between the small initial vortex sheet shape and the circulation produced at the plate edge. This coupling becomes less sensitive as a larger-scale flow is established.

The error due to the start-up with velocity smoothing can be made arbitrarily small by taking a fixed number of initial time steps which are arbitrarily small. For example, we take a uniform time step $\Delta t = KC/1200$, and use $\delta_1 = 10^{-3}$ for the first 20 time steps and obtain vortex spirals with one complete turn and total circulation 0.024. Reducing Δt to $KC/4800$, we can reduce δ_1 to 3×10^{-4} . Since δ_1 is small, this initial uniform smoothing causes errors which are relatively insignificant. The time step can be gradually increased once the initial vortex spiral is established.

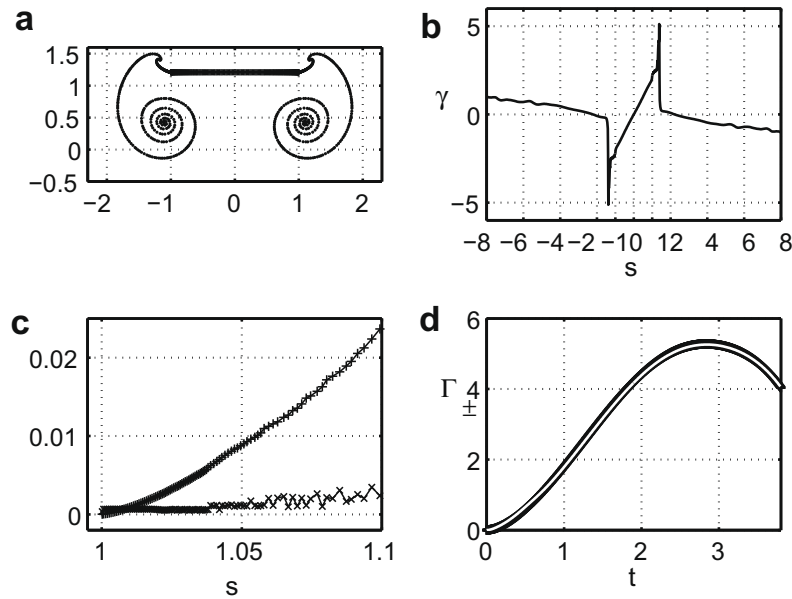


Fig. 10. (a) The position of the plate and free vortex sheets at time $t = KC$. (b) The distribution of γ versus s at time $t = KC$. (c) The vortex sheet smoothing parameter $\delta_t(s)$ (plusses) and the spacing between points (crosses) plotted versus arc length s near one edge of the plate. (d) The total circulation versus time for the tapered-smoothing case (thick black line) and the velocity-smoothed case (overlaid white line) of Fig. 9.

Table 2

Maximum circulation in the tapered smoothing method ($|\Gamma^t(t)|$) compared with velocity smoothing ($|\Gamma^v(t)|$) and standard smoothing ($|\Gamma^s(t)|$) methods for the benchmark problem of Section 2.

Δt	δ_0	$\text{Max} \Gamma^t(t) $	$\text{Max} \Gamma^v(t) $	$\text{Max} \Gamma^s(t) $
2KC/600	0.2	5.2734	5.2692	5.7432
2KC/600	0.1	5.2971	5.3061	5.5859
2KC/600	0.05	5.2897	5.3075	5.4940
2KC/600	0.025	5.2849	5.2939	5.4337

In Fig. 10 we show the result of this method for the oscillating plate problem considered in Section 2. We use $\delta_0 = 0.2$ and $\eta = 2\delta_0 = 0.4$. The value of η is large enough to obtain quadratic convergence as $\delta_0 \rightarrow 0$; see Section 4.2. In Fig. 10(a) we obtain a sheet shape which is more similar to that in Fig. 9(a) than to the shapes with uniform delta-smoothing, Fig. 1. The distribution of vorticity in Fig. 10(b) is also very similar to that in Fig. 9(b). There is an 8% difference in the peak values of vorticity in the two curves. Because the peak is very sharp, this value is sensitive to small deviations in the dynamics of the flows. In Fig. 10(c) the spacing between points in the plus sheet near the plate edge at $s = 1$ is shown (crosses) together with the values of vortex sheet smoothing $\delta_t(s)$ (plusses). The spacing is significantly smaller than $\delta_t(s)$ except very close to the edge, where the points are the “gap points” defined previously, used only as sources of vorticity (to have a smooth mesh), and not evolved forward with the Birkhoff–Rott equation. In Fig. 10(d) we compare the total circulation with the case of velocity smoothing (Fig. 9(d)), and find very good agreement.

In Table 2, we list the maximum circulation shed for the tapered smoothing case (Γ^t) at four values of δ_0 , and compare the values with those for the velocity smoothing case (Γ^v) and standard smoothing (Γ^s). Despite significant differences in Algorithms 2 and 3, there is good agreement between Γ^t and Γ^v with relative error of about 2×10^{-3} . As stated previously, this level of error is associated with the initial approximation of the self-similar spiral during the impulsive acceleration of the plate. In Appendix A we give similar data for the wake half-width, and find that the convergence of the tapered smoothing and velocity smoothing methods are superlinear while the convergence of the standard smoothing method is sublinear.

7. Summary and conclusions

We have studied numerical methods for computing vortex sheet separation for a simple solid body, a rigid plate. Earlier studies have regularized the vortex sheet in a way that gives discontinuous solutions and errors that converge nonuniformly and slowly (like a square root) in the regularization parameter. We have proposed two numerical methods for improving convergence. They were analyzed first through a model problem, which shows improved convergence rates in the smoothing

parameters. The discontinuous vorticity becomes continuous, and the square root convergence is improved to a quadratic convergence or a 3/2-power convergence in a much smaller smoothing parameter (δ_1 , proportional to the time step). We then proposed time-stepping algorithms for the methods, and found much-improved accuracy relative to the earlier methods for similar computational expense.

Acknowledgment

We would like to acknowledge the support of NSF Division of Mathematical Sciences Grant 0810602.

Appendix A. Convergence rates

In Table A.1, we list the wake half-widths at $t = 3.8$ for the tapered smoothing case (ζ^t), the velocity smoothing case (ζ^v), and the standard smoothing case (ζ^s) at four values of δ_0 . In the last two rows, the number in parentheses is the power-law rate of convergence α when the error is assumed to be proportional to δ_0^α . The exponent α is estimated from the adjacent value of the wake half-width and the values for the two coarser meshes. The convergence rate exponents are in the range of 1.3–2.3 for the tapered smoothing and velocity smoothing methods; both are greater than the standard smoothing exponent, which averages about 0.3.

In Fig. A.1, after an initial transient of larger error, errors are reduced by a factor of approximately 4 with each halving of the time step, indicating convergence that is second-order in Δt .

In Fig. A.2 we find third-order convergence with respect to the number of Chebyshev modes m . The reason is that a locally-second-order (globally third-order) quadrature rule is used over one subinterval of the integrals on the right hand side of Eq. (20).

Table A.1

Wake half-width at $t = 3.8$ in the tapered smoothing method (ζ_+^t) compared with velocity smoothing (ζ_+^v) and standard smoothing (ζ_+^s) methods for the benchmark problem of Section 2.

Δt	δ_0	Max(Re ζ_+^t)	Max(Re ζ_+^v)	Max(Re(ζ_+^s))
2KC/600	0.2	1.8370	1.8295	2.0581
2KC/600	0.1	1.8626	1.8575	2.0142
2KC/600	0.05	1.8727 (1.34)	1.8685 (1.35)	1.9758 (0.193)
2KC/600	0.025	1.8748 (2.27)	1.8713 (1.97)	1.9461 (0.371)

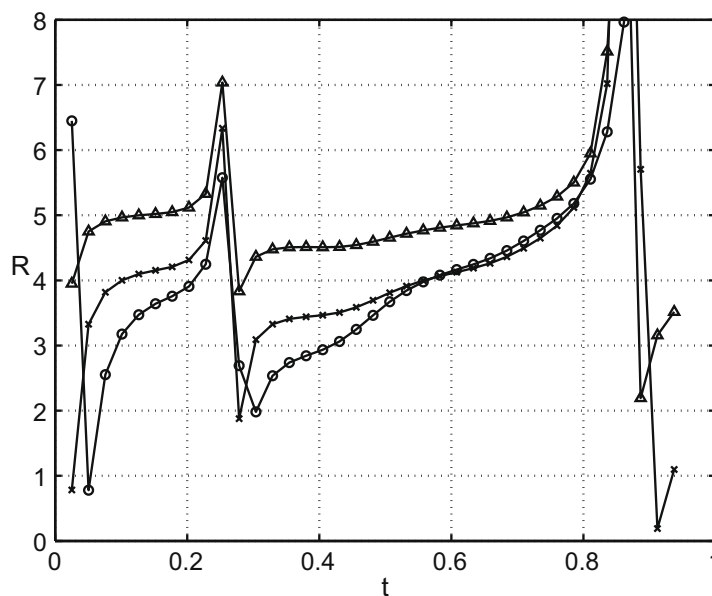


Fig. A.1. Successive ratios of errors in $\Gamma_-(t)$ for the problem in Section 3 as $\Delta t_k = KC \times 2^{-k}/150$, $k = 0, 1, 2, 3, 4$. Denoting the value of $\Gamma_-(t)$ computed with Δt_k as $\Gamma_-^k(t)$, plotted is $R = |\Gamma_-^k(t) - \Gamma_-^4(t)| / |\Gamma_-^{k+1}(t) - \Gamma_-^4(t)|$ for $k = 0$ (circles), 1 (crosses), and 2 (triangles). Second-order convergence gives values between 4 and 5.

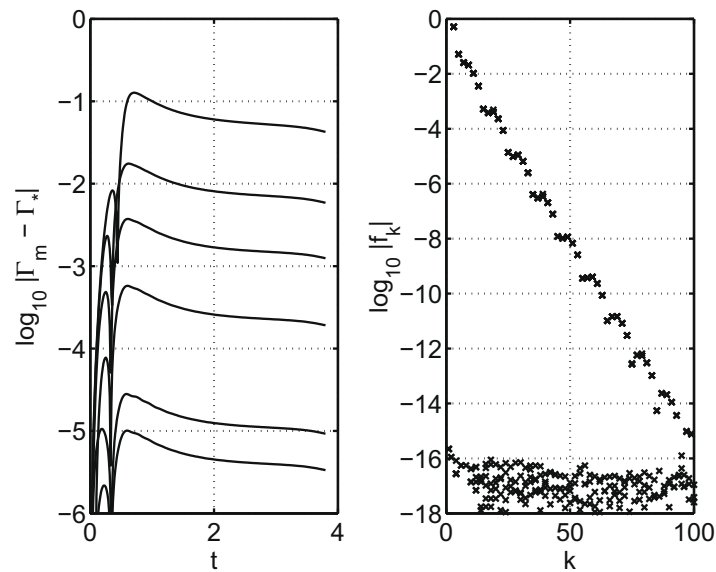


Fig. A.2. (a) Difference between $\Gamma_*(t)$ for the problem in Section 3 as the number of Chebyshev modes m is varied. Denoting the value of $\Gamma_*(t)$ computed with m as $\Gamma_m(t)$, plotted is $|\Gamma_m(t) - \Gamma_*^{1280}(t)|$ over $0 \leq t \leq KC = 3.8$ for $m = 20, 40, 80, 160, 320, 640$. Convergence is approximately third-order in m . (b) Spectrum of Chebyshev modes $|f_k|$ at time $t = KC$. The decay of the modes is exponential.

References

- [1] G.K. Batchelor, An Introduction to Fluid Dynamics, Cambridge University Press, Cambridge, 1967.
- [2] P. Saffman, Vortex Dynamics, Cambridge University Press, Cambridge, 1992.
- [3] M. Jones, The separated flow of an inviscid fluid around a moving flat plate, *J. Fluid Mech.* 496 (2003) 405–441.
- [4] R. Krasny, Desingularization of periodic vortex sheet roll-up, *J. Comput. Phys.* 65 (1986) 292–313.
- [5] R. Krasny, Computation of vortex sheet roll-up in the Trefftz plane, *J. Fluid Mech.* 184 (1987) 123–155.
- [6] R. Krasny, Vortex sheet computations: roll-up, wakes, separation, *Lect. Appl. Math.* 28 (1991) 385–402.
- [7] M. Nitsche, R. Krasny, A numerical study of vortex ring formation at the edge of a circular tube, *J. Fluid Mech.* 276 (1994) 139–161.
- [8] A.J. Chorin, P.S. Bernard, Discretization of a vortex sheet, with an example of roll-up (for elliptically loaded wings), *J. Comput. Phys.* 13 (1973) 423–429.
- [9] L. Rosenhead, The point vortex approximation of a vortex sheet, *Proc. Roy. Soc. London Ser. A* 134 (1932) 170–192.
- [10] R.K. Shukla, J.D. Eldredge, An inviscid model for vortex shedding from a deforming body, *Theor. Comput. Fluid Dyn.* 21 (5) (2007) 343–368.
- [11] J. Peng, J. Dabiri, Optimal stroke patterns for a model jellyfish swimmer with thin, flexible body, in: American Physical Society, 60th Annual Meeting of the Division of Fluid Dynamics, November 18–20, 2007, Abstract# EH. 004, 2007.
- [12] S. Alben, M.J. Shelley, Flapping states of a flag in an inviscid fluid: bistability and the transition to chaos, *Phys. Rev. Lett.* 100 (2008) 074301.
- [13] S. Alben, Simulating the dynamics of flexible bodies and vortex sheets, *J. Comput. Phys.* 228 (7) (2009) 2587–2603.
- [14] C.E. Brown, W.H. Michael, Effect of leading edge separation on the lift of a delta wing, *J. Aero. Sci.* 21 (10) (1954).
- [15] L. Cortelezzi, A. Leonard, Point vortex model of the unsteady separated flow past a semi-infinite plate with transverse motion, *Fluid Dyn. Res.* 11 (6) (1993) 263–295.
- [16] S. Michelin, S.G. Llewellyn Smith, B.J. Glover, Vortex shedding model of a flapping flag, *J. Fluid Mech.* 617 (2008).
- [17] T. Sarpkaya, R.L. Schoaff, Inviscid model of two-dimensional vortex shedding by a circular cylinder, *AIAA J.* 17 (11) (1979) 1193–1200.
- [18] M. Nitsche, Scaling properties of vortex ring formation at a circular tube opening, *Phys. Fluids* 8 (7) (1996) 1848–1855.
- [19] G.H. Keulegan, L.H. Carpenter, Forces on cylinders and plates in an oscillating fluid, *J. Res. Nat. Bureau Stand.* 60 (5) (1958) 423–440.
- [20] M.A. Golberg, Numerical Solution of Integral Equations, Plenum Press, New York, 1990.
- [21] R. Krasny, A study of singularity formation in a vortex sheet by the point-vortex approximation, *J. Fluid Mech.* 167 (1986) 65–93.
- [22] A. Ralston, P. Rabinowitz, A First Course in Numerical Analysis, Dover, 2001.
- [23] D.I. Pullin, The large-scale structure of unsteady self-similar rolled-up vortex sheets, *J. Fluid Mech.* 88 (03) (1978) 401–430.